

Retrieval of cloud properties from thermal infrared radiometry using convolutional neural network



Quan Wang^a, Chen Zhou^{a,b,*}, Xiaoyong Zhuge^c, Chao Liu^{d,e}, Fuzhong Weng^f, Minghuai Wang^{a,b}

^a School of Atmospheric Sciences, Nanjing University, Nanjing 210023, China

^b Joint International Research Laboratory of Atmospheric and Earth System Sciences and Institute for Climate and Global Change Research, Nanjing University, Nanjing 210023, China

^c Key Laboratory of Transportation Meteorology of China Meteorological Administration, Nanjing Joint Institute for Atmospheric Sciences, Nanjing 210041, China

^d Collaborative Innovation Center on Forecast and Evaluation of Meteorological Disasters, Nanjing University of Information Science and Technology, Nanjing 210044, China

^e Key Laboratory for Aerosol-Cloud-Precipitation of China Meteorological Administration, School of Atmospheric Physics, Nanjing University of Information Science and Technology, Nanjing 210044, China

^f State Key Laboratory of Severe Weather, Chinese Academy of Meteorological Sciences, Beijing 100081, China

ARTICLE INFO

Edited by Menghua Wang

Keywords:

Cloud optical properties
Convolutional neural network
Remote sensing
Diurnal cycle

ABSTRACT

In this study, a deep learning algorithm is developed to consistently retrieve the daytime and nighttime cloud properties from passive satellite observations without auxiliary atmospheric parameters. The algorithm involves the thermal infrared (TIR) radiances, viewing geometry, and altitude into a convolutional neural network (denoted as TIR-CNN), and retrieves the cloud mask, cloud optical thickness (COT), effective particle radius (CER), and cloud top height (CTH) simultaneously. The TIR-CNN model is trained using daytime Moderate Resolution Imaging Spectroradiometer (MODIS) products during a full year, and the results are validated and evaluated using passive and active products observed in independent years. The evaluation results show that the cloud properties retrieved by the TIR-CNN are well consistent with all available MODIS day-time products (cloud mask, COT, CER, and CTH) and night-time products (cloud mask and CTH). The retrieved COT and CTH also show good agreements with active sensors for both daytime and nighttime, indicating that the algorithm performs stably in the diurnal cycle.

1. Introduction

Clouds influence the Earth's climate system through modulating the spatiotemporal distribution of the planetary radiation budget and impact the hydrological cycle through precipitation (Boucher et al., 2013; Stevens and Bony, 2013). Spatiotemporal changes in cloud optical and microphysical properties contribute significantly to the uncertainties in quantifications and interpretations of climate change (Leinonen et al., 2019). The cloud optical thickness (COT), effective particle radius (CER), and top height (CTH) are essential variables that have crucial impacts on the Earth's net radiation due to their distinct scattering and absorption properties (Fauchez et al., 2018; Kiehl et al., 1994; Min et al., 2020; Wang et al., 2016b). Therefore, an accurate understanding of these properties and their spatiotemporal changes is

important for determining their roles in the Earth's climate system.

With the characteristics of the long historical record, high temporal resolution, and the large spatial coverage, the passive satellite observations have become one of the primary means of monitoring the cloud optical and microphysical properties at different spatial and temporal scales. Over the past several decades, many progresses have been made in the retrievals of these data products from satellites (Twomey and Cocks, 1982; Baum et al., 2005; Yang et al., 2015). Nakajima and King (1990) developed a seminal algorithm for COT and CER retrievals, which can be referred to as the bi-spectral solar reflectance method. Following the success of this method, many different attempts have been made to explore the accurate estimation of the cloud parameters, with different constraints in spectral channels, particle habits (for ice clouds), and particle distributions (King et al., 1992; Letu et al., 2020; Minnis

* Corresponding author at: School of Atmospheric Sciences, Nanjing University, Nanjing 210023, China.

E-mail address: czhou17@nju.edu.cn (C. Zhou).

et al., 2011, 2021; Platnick et al., 2001, 2003, 2017; Tang et al., 2017; Teng et al., 2020; Zhuge et al., 2021). The basic physical principle behind this method is that the cloud radiances measured by the nonabsorptive channels in the visible or near-infrared (VIS/NIR) wavelength are primarily affected by COT, while those in water-absorption channels (i.e. shortwave infrared wavelength, SWIR) are sensitive to the CER (Nauss and Kokhanovsky, 2011). COT and CER can be retrieved from the satellite measurements of two VIS/NIR and SWIR channels. These solar radiation-based methods are efficient to obtain acceptable retrievals of cloud properties for the passive satellites, but only for daytime scenes. The inherent problems still exist in nighttime conditions, polar regions, and optically thin cloud retrievals (Fauchez et al., 2018). Compared with passive sensors, active sensors are less affected by the diurnal cycle, so lidar and radar measurements can be used to evaluate the diurnal variations of the cloud properties. However, active observations are not suitable for high temporal monitoring as a result of sparse coverage and satellite quantity (Lai et al., 2019).

Without solar radiation, the nighttime estimations of cloud properties remain a challenging task but are critical for investigating the diurnal variations of cloud-climate feedback (Gong et al., 2018). With TIR measurements, the split-window method described by Inoue (1985) was introduced to provide cloud products (e.g. COT, CER, and cloud phase) for both daytime and nighttime scenes, which inspired a lot of attempts and improvements (Duda and Spinhirne, 1996; Hamada and Nishi, 2010; Heidinger and Pavolonis, 2009; Iwabuchi et al., 2018; Parol et al., 1991; Yang et al., 2005). The split-window method retrieves the cloud properties based on the difference between brightness temperature (BT) from different window channels. Despite the extended application for nighttime scenes and the good performance on optically thin clouds, this method becomes problematic for opaque thick cloud cases. Wang et al. (2016a, 2016b) proposed an infrared-based optimal estimation (OE-IR) method to infer the ice cloud properties for Moderate Resolution Imaging Spectroradiometer (MODIS) based on an optimal estimation method. The OE-IR is a useful method to supplement the absence of the products during the period of nighttime through the consistent retrievals and achieve comparable results for COT and CTH. However, it still suffers from biases in CER retrievals and COT retrievals of optically thick cloud layers ($COT > 10$) (Wang et al., 2016b). Libois and Blanchet (2017) added far-infrared ($\geq 15 \mu\text{m}$) measurements to the optimal estimation methods to improve the retrieval ability for clouds with large optical thickness, with large particles, and in polar regions. Saito et al. (2020) further reduced the retrieval uncertainties of ice clouds in the diurnal variation by accounting for the middle-to-far-infrared measurements, temperature dependence, and ice particle habits, which improved the estimations for the optically thick clouds. Besides, the TIR measurements also have the substantial ability to infer CTH. Since the opacity of CO_2 is sensitive to the wavelength from 13 to 15 μm , the height of mid-to high-level clouds can be inferred by the CO_2 -slicing algorithm (King et al., 1992; Baum et al., 2012). The addition of the IR window measurements helps the estimations of low-level layers considering the BT discrepancy in clear-sky and cloudy observations (Menzel et al., 2008).

As mentioned in Marchand et al. (2010), optically thick clouds are widely distributed over the globe, which is considered to be an important modulator of the radiative budget of the Earth. Currently, TIR-based algorithms inherently perform poorly for optically thick clouds (Iwabuchi et al., 2014; Wang et al., 2016a). Though far-infrared radiometry or synergistic satellite measurements are helpful in several studies (Gong et al., 2018; Libois and Blanchet, 2017; Saito et al., 2017, 2020), the former is not accessible in most space-borne instruments and the latter may introduce extra noises. Moreover, the complicated processes of radiative transfer calculations involved in solar reflectance-based and TIR-based algorithms are usually more computationally expensive.

In recent years, deep learning techniques, with the improvement of computational resources and the increasing amount of satellite observations, have attracted widespread attention in remote sensing

applications (i.e., Yuan et al., 2020). As shown in numerous attempts, deep learning methods show great potential in spatiotemporally establishing the complex and nonlinear relationship between the in situ measurements and the targets, such as the applications of classifying remote sensing imageries and quantifying environmental parameters (Håkansson et al., 2018; Lang et al., 2019; Li et al., 2020; Wang et al., 2020; Wieland et al., 2019). Different from conventional physical models, convolutional neural networks (CNNs) have the ability to account for statistical relationships between input variables and targets, capture the spatial variations of input features, and reduce the computational burden. In addition, CNN can obtain spatial information from horizontally inhomogeneous clouds, which can be used in cloud property retrievals. Hence, a CNN-based algorithm (TIR-CNN) is proposed to investigate the cloud properties in diurnal variation from TIR measurements in this paper.

The primary goal of this study is to develop a CNN model to continuously retrieve the cloud optical properties (i.e. COT, CER, and CTH) for the passive satellite in the diurnal cycle. The TIR-CNN model maps the high-quality daytime results to nighttime scenes by establishing a robust relationship to the MODIS TIR (8–14 μm) measurements. The performance is examined by the standard MODIS cloud products and the active measurements, and the generalization ability is also discussed in the spatial and temporal scales. Datasets, retrieval algorithm, and evaluation metrics are briefly introduced in Section 2; In Section 3, the performance of the model is evaluated using the MODIS products and active measurements. Conclusions and discussions are presented in Section 4.

2. Data and methodology

2.1. Data

2.1.1. MODIS data

The MODIS imager onboard the polar-orbiting Aqua (1:30 pm) satellite was launched in 2002. It provides long-term and large-scale measurements of the Earth-atmosphere system with 36 spectral channels covering 0.4–14.4 μm . The required Aqua-MODIS products, i.e. MYD021KM, MYD03, MYD35, and MYD06, with the spatial resolution of 1 km can be obtained on Level 1 and Atmosphere Archive and Distribution System website (<https://ladsweb.modaps.eosdis.nasa.gov/>). The TIR measurements are not only sensitive to the optically thin clouds but also continuously obtained in the diurnal cycle as they are independent of the solar geometry (Fauchez et al., 2018). In this study, TIR radiations from Aqua-MODIS collection 6.1 (C6.1) Level 1B calibrated radiances product (MYD021KM) are used to infer cloud properties in both daytime and nighttime. Meanwhile, the satellite viewing zenith angles (VZA) and altitude from the geolocation product (MYD03) are also used to build the retrieval model, and the geolocation information is collected to co-locate data observed by different satellites. The cloud mask product (MYD35_L2) is selected to train a classifier to screen out the cloud-contaminated pixels. MODIS cloud optical and physical parameters (i.e., COT, CER, and CTH) with high quality (King et al., 2003; Platnick et al., 2017), from the MODIS Level-2 cloud product (MYD06_L2), are used in the training and testing processes of our model. No ancillary meteorological data is incorporated in the CNN model, so the results are not affected by inherent errors of external ancillary datasets.

2.1.2. Independent validation products

The performance of the proposed algorithm is extensively evaluated and analyzed with the measurements of CALIOP (Cloud-Aerosol Lidar with Orthogonal Polarization). CALIOP is an active lidar instrument onboard the CALIPSO (Cloud-Aerosol Lidar and Infrared Pathfinder Satellite Observations) satellite. It was placed into orbit in 2006 (Winker et al., 2007). The CALIPSO and Aqua were both included in the “A-train” constellation orbited at the altitude of 705 km before the year of 2018.

Table 1

Summary of MODIS data sources and preprocessing parameters.

Sensors	Product name	Spatial Resolution	Variables	Mean	S.D.*	Unit
MODIS	MYD021KM	1 km	Band 29	5.557	2.356	W/(m ² μm sr)
		1 km	Band 31	6.286	2.269	W/(m ² μm sr)
		1 km	Band 32	5.952	1.988	W/(m ² μm sr)
		1 km	Band 33	4.222	0.936	W/(m ² μm sr)
		1 km	Band 34	3.550	0.635	W/(m ² μm sr)
		1 km	Band 35	3.114	0.451	W/(m ² μm sr)
MYD03	1 km	$\cos\theta^*$	0.809	0.172	–	–
	1 km	Altitude	0.292	0.733	km	–
MYD06	1 km	COT	6.535	11.388	–	–
	1 km	CER	11.966	12.085	μm	–
MYD35	1 km	CTH	3.048	4.152	km	–
	1 km	Cloud Mask	–	–	–	–

Note: * S.D. Standard deviation; $\cos\theta$ the cosine of VZA.

The CALIPSO lagged the Aqua by about 1-2 min, making it possible to co-locate the synergistic measurements. For a comprehensive analysis, the number of cloud layers, the layer-integrated backscatter of the cloud layer, and the cloud top height information are extracted from CALIPSO Lidar level-2 1 km (V4.20) cloud layer product to intercompare with the nighttime retrieval results.

2.1.3. Data preprocessing

Considering the overlap of solar and infrared spectra (Zhang et al., 2018), and artificial cross detector striping of some channels (Fig. S1) (Rakwatin et al., 2007), six TIR channels (8.58 μm, 10.98 μm, 11.89 μm, 13.28 μm, 13.69 μm, and 13.83 μm) greater than 8 μm (Wang et al., 2016b; Iwabuchi et al., 2016; Libois and Blanchet, 2017), together with VZA and altitude data are used as input variables to the model. MODIS level-2 cloud mask, COT, CER, and CTH data are treated as targets to train, validate and test the model. On account of different retrieval failure rates of COT and CER products and the detectors' functional issues in VNSWIR (visible, near-, or shortwave-infrared channels of 0.66 μm, 0.86 μm, or 1.2 μm, respectively)-1.6 μm products (Cho et al., 2015), COT and CER from VNSWIR-2.1 μm and VNSWIR-3.7 μm products are pixel-level averaged to derive the robust labels for the regression model.

To improve the retrieval accuracy and reduce the training period, the training data are transformed to have a standard normal distribution with mean 0 and standard deviation 1 using the z-score method, which is shown below:

$$z = \frac{x - \mu}{\sigma} \quad (1)$$

where x indicates the inputs and ground truth variables, μ and σ are mean and standard deviation values of x , respectively. In this manner, different features are normalized to the same magnitude to simplify the learning process and avoid exploding gradients in the training. These

Table 2

Summary of data sets used in this study.

Dataset	Count	Day/Night-Time	Size	Period
Training dataset	1,888,680	Daytime	256 × 256	2010
Validation dataset	191,520	Daytime	256 × 256	10-day intervals in 2011
Testing dataset	191,680 191,080	Daytime Nighttime	256 × 256	10-day intervals in 2009

normalization parameters are stored and used to rescale back to the initial distribution space. Unsuccessful retrievals are assigned as not available numbers (NAN) in backpropagation. Table 1 summarizes the related data and parameters used in preprocessing.

To cover as much of the Earth's surface and viewing geometries as possible and respond to seasonal variation, full-year granules of 2010 are collected to build the training dataset. The products with the 10-day interval in 2011 are selected as the validation dataset in the training phase. The 10-day-interval data in 2009, which is independent of the training and validation dataset, are obtained as the testing dataset. Due to the memory and computational burden, the granules are split into samples with 256 × 256 km size. After preprocessing, 1,888,680, 191,520, and 382,760 samples are prepared for the training, validation, and testing database, respectively, as summarized in Table 2.

2.2. Development of the TIR-CNN retrieval algorithm

Spatial distributions, optical and microphysical properties of clouds are all determined by the meteorological backgrounds, so cloud properties are statistically connected to the horizontal distribution of clouds. On the other hand, the cloud pixels are not independent at the horizontal scale due to net horizontal radiative transports, especially for high-resolution satellite data (Fauchez et al., 2018; Iwabuchi and Hayasaka, 2003). Therefore, we propose a CNN-based deep learning architecture to capture the statistical features among adjacent pixels of satellite observations as a robust solution for retrieving cloud optical and microphysical properties.

Fig. 1 illustrates the architecture of our TIR-CNN model, which is broadly inspired by the U-Net architecture developed by Ronneberger et al. (2015) for neuronal structure segmentation in the transmitted light microscopy images. This model is an asymmetric model, which is arranged continuously by the same number of encoding and decoding layers (Fig. 1a). The basic convolutional block (Fig. 1b) is stacked by two 2D-convolutional layers (with 3 × 3 kernels). Each convolutional layer is followed by a batch normalization (BatchNorm) layer and a leaky rectified linear unit (LeakyReLU, formally $\text{LeakyReLU}(x) = \max(0, x) + 0.01 \cdot \min(0, x)$). When the input features pass through these layers, multiple-scale features are extracted. As is shown in Fig. 1c, a down-sample block is constructed by a convolutional block and a 2 × 2 max-pooling layer. The latter is used to extract the maximum value of a receptive field to reduce the spatial size. In an up-sample block (Fig. 1d), half of the upsampling features from a transposed convolutional layer (2 × 2 kernels) are concatenated with the shallow features by skip-connection (\oplus in Fig. 1d). Several stacked down-sample blocks with continuous doubling nodes (encoding layers) are designed to capture the abstract representations and reduce the computational burden. As the symmetrical part, the decoding layers with the same number of nodes aim to recover the initial feature size and increase the network depth via a sequence of up-sample blocks. In the last layer, point-wise convolutions are applied to transform the superior features to the desired targets (COT, CER, and CTH) or cloud classification, and this forward propagation can be described as:

$$\hat{y}(x, \omega, b) = f_i(\omega_i f_{i-1}(\dots f_1(\omega_1 x + b_1) \dots) + b_i) \quad (2)$$

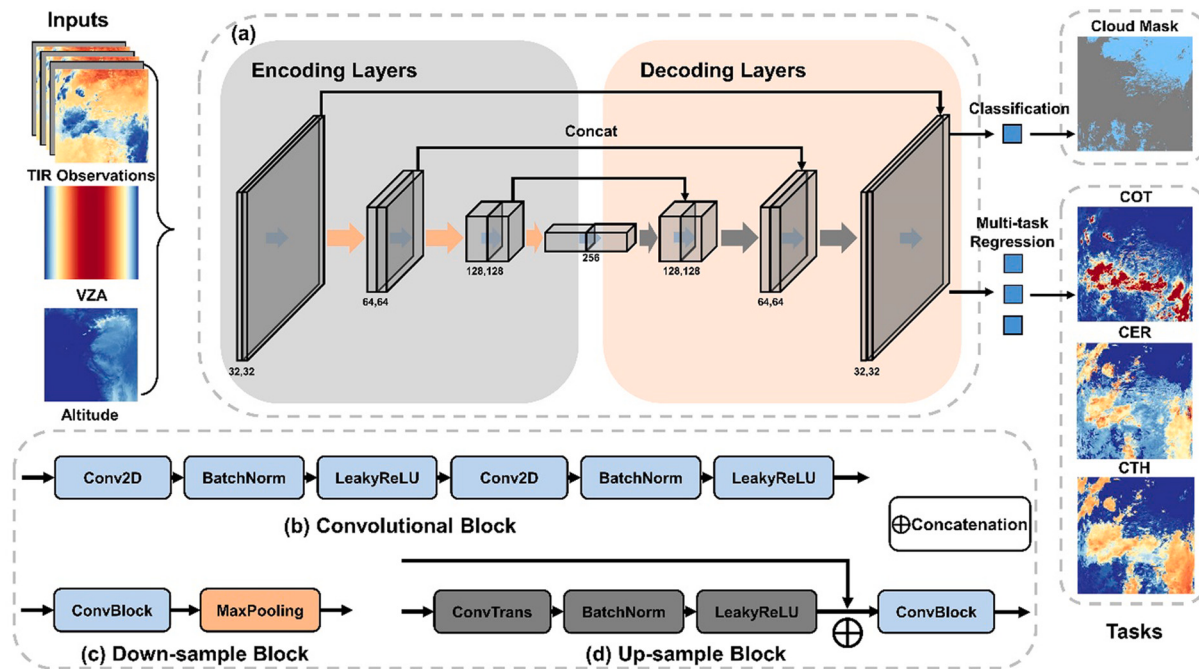


Fig. 1. The architecture of the TIR-CNN model. (a) The simple model architecture consists of encoder and decoder parts. (b) The operations within a basic convolutional block. (c) The operations within a down-sample block. (d) The operations within an up-sample block where \oplus means concatenation.

where $\hat{y}(x, \omega, b)$ represents the output cloud properties, and is calculated as the label's probability by the softmax function $p_c = \frac{e^{\hat{y}_c}}{\sum_{n=0}^N e^{\hat{y}_n}}$ for cloud identification; f defines the transformation of the nonlinear activation function; ω_i and b_i are the weight matrix and bias vector for i_{th} layer, respectively.

This architecture has the advantages of lower training data requirements and relatively less trainable parameters (about seven million parameters) as discussed in Ronneberger et al. (2015) and Long et al., 2015. To balance the retrieval accuracy and model size, the network is determined as the combination of three encoding layers (with 32, 64, and 128 nodes), one 256-nodes convolutional block, and three mirrored decoding layers. The input variables are fed into the model to capture context and learn the complex nonlinear relationship according to the errors between the outputs and targets (y). The loss functions of regression and segmentation tasks are defined as:

$$l(\hat{y}, y) = \frac{1}{M} \sum_{j=1}^M \log(\cosh(\hat{y}_j - y_j)) + \frac{\lambda}{M} \sum \omega_i^2 \quad (3)$$

$$l_{mask}(y, p) = -\frac{1}{M} \sum_{j=1}^M (y_j \bullet \log p_j + (1 - y_j) \bullet \log(1 - p_j)) + \frac{\lambda}{M} \sum \omega_i^2 \quad (4)$$

where y is the truth cloud parameters (taking a value of 1 or 0 for cloudy or clear in cloud identification), M denotes the number of samples, \hat{y} is the estimated cloud property, the last penalty term represents the L2 regularization ($\lambda=0.01$) for the feature weights (ω) to reduce the errors and avoid overfitting. Multi-task regression can discover the potential relatedness between tasks without explicit supervised constraints, which helps to improve upon generalization, reduce the risk of overfitting and achieve better performance (Caruana, 1997). Therefore, the COT (τ), CER (r), and CTH (h) are simultaneously trained by updating the sharing parameters according to minimizing the total loss (L), which can be written as:

$$L = a_\tau l_\tau + a_r l_r + a_h l_h \quad (5)$$

where a_τ , a_r , and a_h are the relative weights for the loss of COT (l_τ), CER

(l_r), and CTH (l_h), respectively, which are adjusted adaptively to balance the contribution of each term.

During training, all weights in convolutional kernels are initiated by Kaiming Initialization (He et al., 2015), and are optimized by the Adam (Adaptive Moment Estimation) gradient descent optimizer with the default parameters ($\beta_1 = 0.9$, $\beta_2 = 0.999$) (Kingma and Ba, 2014). The learning rate is empirically set as 0.001 and further tuned by a multi-step decay strategy with a decay rate of 10, which accelerated the training processes efficiently. Different amounts of dataset and input features have been attempted in this study, the comparisons of evaluation results show that a full-year dataset makes the model slightly more stable in time series, but with limited improvement by adding input TIR channels (Fig. S2). All experiments are performed on a platform with an Intel Xeon (2.00 GHz, 26 cores) CPU, and several NVIDIA GeForce GTX 2080ti GPUs with 10.732 GB RAM. Patches with 32 batch-size are fed into the network for each iteration, and trained until achieves convergence for both the training and validation dataset (Fig. S3). As for the application, the cloud properties for a full MODIS granule can be retrieved on a single GPU within 1 s.

2.3. Performance evaluation and analysis

In this study, the magnitude of forecast errors, the systematic bias errors, and the linear correlation between outputs and standard values are quantitatively assessed via the following statistical metrics: the root mean squared error (RMSE), the mean bias error (MBE), and the Pearson correlation coefficient (R).

$$RMSE = \sqrt{\frac{\sum_{i=1}^N (s_i - p_i)^2}{N}} \quad (5)$$

$$MBE = \frac{\sum_{i=1}^N p_i - s_i}{N} \quad (6)$$

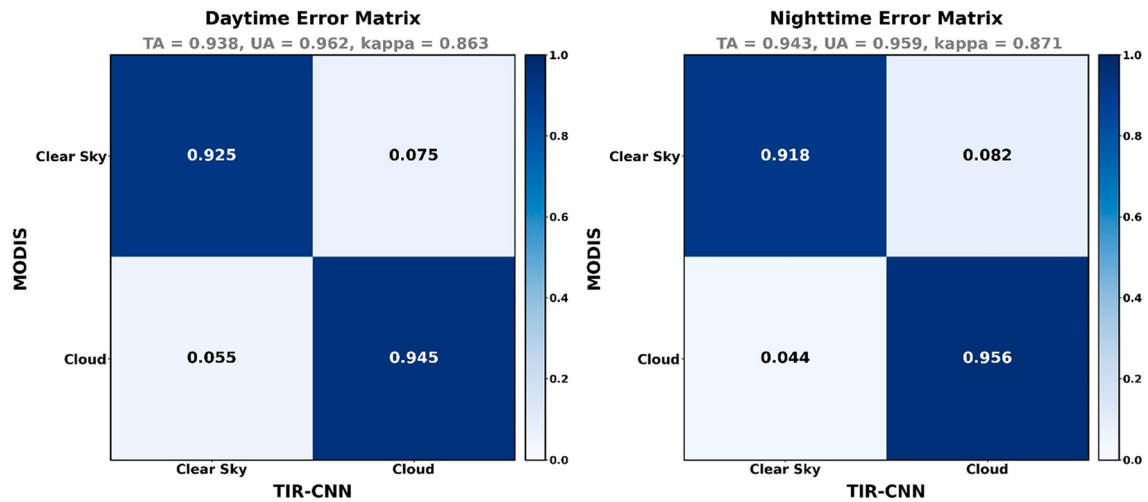


Fig. 2. Error matrices for the TIR-CNN model for cloud detection over the daytime and nighttime.

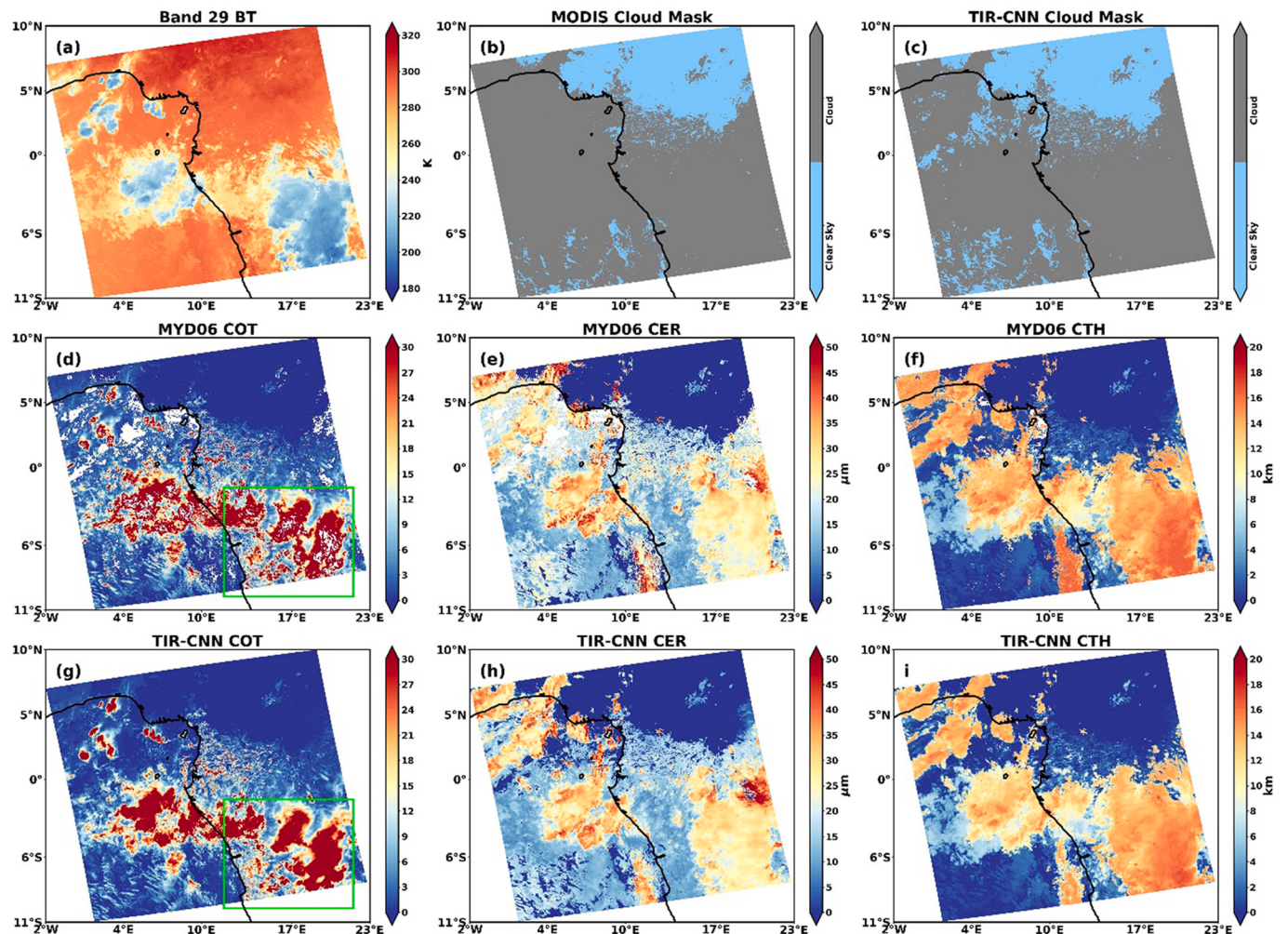


Fig. 3. Comparison of cloud properties obtained from the TIR-CNN model and standard MODIS products for a daytime granule on 1 Jan. 2009 (12:55 UTC). (a) BT image of MODIS band 29. (b, c) are the cloud masks from the MYD35 product and the TIR-CNN model, respectively. (d, e, f) are the COT, CER, and CTH from the MYD06 product, respectively. (g, h, i) are the COT, CER, and CTH from the TIR-CNN model, respectively.

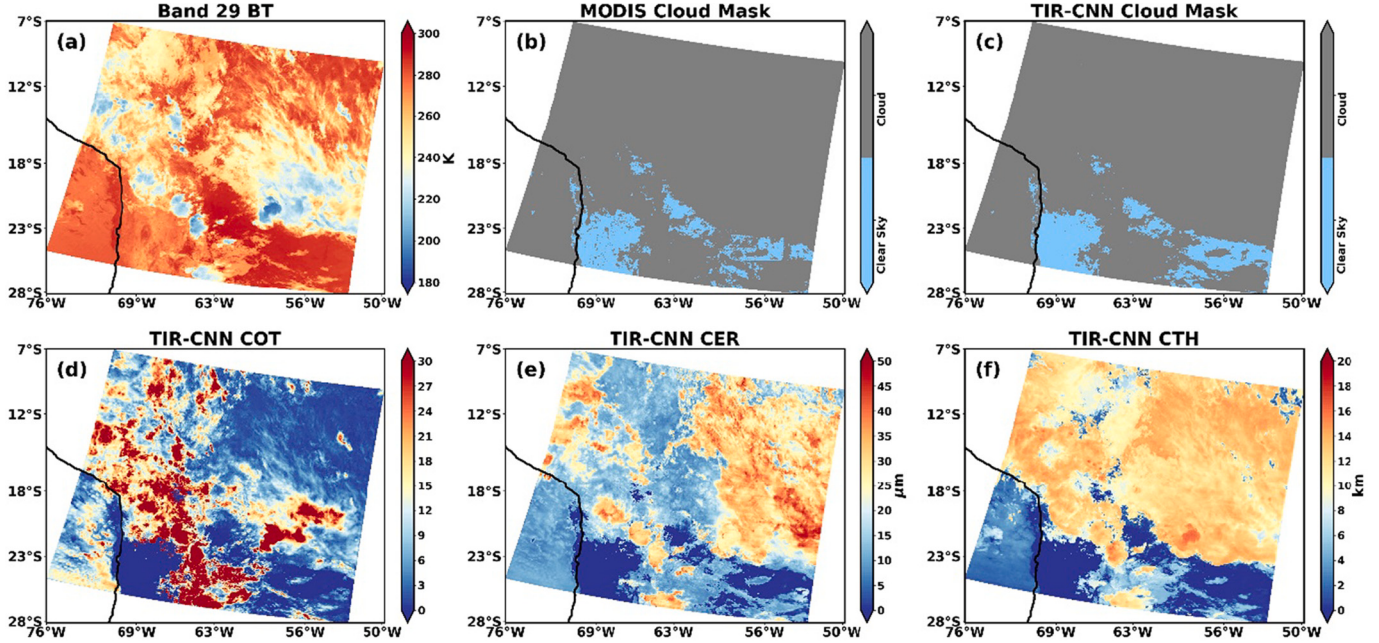


Fig. 4. Similar to Fig. 3, but for a nighttime granule on 1 Jan. 2009 (05:35 UTC). (a) BT image of MODIS band 29. (b, c) are the cloud masks from the MYD35 product and the TIR-CNN model, respectively. (d) COT retrieved from the TIR-CNN model. (e) CER retrieved from the TIR-CNN model. (f) CTH retrieved from the TIR-CNN model.

$$R = \frac{\sum_{i=1}^N (p_i - \bar{p})(s_i - \bar{s})}{\sqrt{\left(\sum_{i=1}^N (p_i - \bar{p})^2 \right)} \sqrt{\left(\sum_{i=1}^N (s_i - \bar{s})^2 \right)}} \quad (7)$$

where N is the total number of calculated pixels, s and p are the standard and predicted cloud properties, respectively. They are calculated against the official products or the active satellite measurements. It should be noted that the selected granules in the test phase should be carried out based on the principle that they are never used in the training or validation set.

3. Results and discussions

The output cloud properties are filtered by the derived cloud mask from the classifier that has competitive results. The total accuracy, producer's accuracy, user's accuracy, and Kappa coefficient (Eq. S1-S5) for daytime and nighttime are 0.938, 0.945, 0.962, 0.863 and 0.943, 0.956, 0.959, 0.871, respectively (Fig. 2). In the testing phase, the standard MODIS cloud products and the CALIPSO cloud layer products in 2009 are collected to reveal the recovery ability and performance of the TIR-CNN model in both daytime and nighttime. 191,680 daytime and 191,080 nighttime samples are selected for the testing dataset, which are independent of the training and validation dataset to make the testing result more convincing.

3.1. Experiments in daytime and nighttime

As an imagery regression task, case study analyses are necessary to investigate the ability of the TIR-CNN model to reproduce geographical patterns of cloud properties. Cases of cloud property retrievals are directly shown as geographical maps. In BT maps, clear sky observations are usually featured by higher BT values, while the cloudy areas are opposite, as the cloud top temperature is usually much lower than the surface.

For the daytime comparison, an Aqua-MODIS granule, which was observed at 12:55 UTC on January 1st, 2009 and located in West Africa

near the equator with the range of (11°S-10°N, 2°W-23°E), is presented to illustrate the daytime retrieval performance (Fig. 3). According to the BT distribution in Fig. 3a, the lower right and middle left parts in the scene are covered by thick clouds, while there are notable cirrus clouds around them over the lower part. The TIR-CNN model can successfully retrieve for almost all clouds (Fig. 3b and c). Fig. 3(d, e, f) are the MYD06 cloud products (COT, CER, and CTH), and Fig. 3(d, h, i) show the corresponding cloud properties from the TIR-CNN model. For this scene, the CNN-derived retrievals are not only consistent with MYD06 products in spatial patterns, but also agree well with the magnitudes of results (Fig. 3d and g). Slight retrieval bias of CER occurs for optically thin clouds ($\text{COT} < 10$), especially for those at the edge of stratiform clouds (Fig. 3e and h). According to Fig. 3f and i, the derived CTH is highly consistent with the MYD06 product (only slight underestimations near 16 km). It should be noted that the CNN retrieval results can reasonably impute the missing values in MODIS products, which is illustrated in the rectangle areas of the COT comparison.

The deep-learning algorithm is statistical, and the physical processes are underlying behind the statistics (Fig. S4). A sensitivity analysis is performed to explore the importance of cloud spatial information in cloud property retrievals. In the sensitivity analysis, the spatial locations of input variables for the case of Fig. 3 are randomly shuffled to exclude the spatial information of clouds, and the spectral information remains unchanged. After performing the CNN calculations, the retrievals are reordered back to their initial spatial locations (Fig. S5). The differences between Fig. 3 and Fig. S5 suggest that cloud spatial relationships are the key to why the TIR-CNN model can reconstruct the cloud properties well. To illustrate the mathematical mechanism of our TIR-CNN model, four clear features captured by the convolutional kernels in the first layer of each convolutional block are visualized in Fig. S6. Simple features such as cloud shape and edges are initially learned in the shallow layer (as layers 1, 3, and 5), more complex and abstract textures of clouds are learned in higher layers (as layers 7, 9), and it seems that thick clouds and their central parts are learned on the deepest layers (as layers 11, 13). More features are listed in Figs. S7-S13.

Fig. 4 shows a nighttime case covering South America (S: 7°-28°, W: 50°-76°) observed at 05:35 UTC, January 1st, 2009. Only TIR-CNN model retrieved results are presented because no COT or CER product

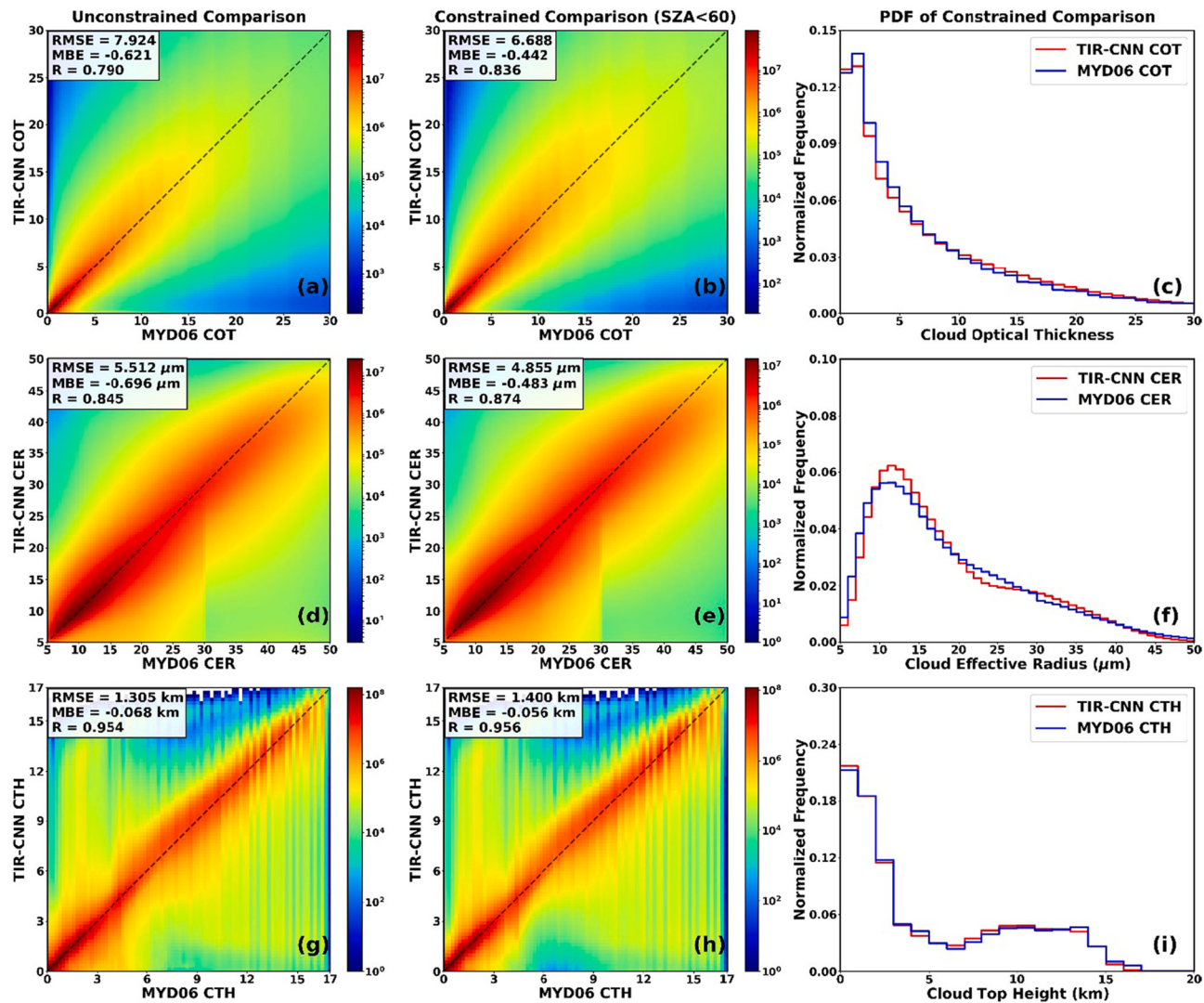


Fig. 5. Pixel-by-pixel comparisons of COT, CER, and CTH from this study with the MYD06 cloud products in 2009 (a, d, and g). Colors denote the number of observations in each respective pixel. Density scatter plots of constrained comparisons with $SZA < 60^\circ$ are shown in b, e, and h. The probability density functions corresponding to (b, e, h) obtained from MYD06 products and CNN-derived results are presented in c, f, and i. All comparable retrievals are defined as simultaneous successfully retrieved in both the TIR-CNN model and MYD06 products.

is provided by MYD06 at night. In this case, optically thick clouds cover most areas (left and central parts) of the scene, surrounded by some thin clouds (Fig. 4a). Similarly, the TIR-CNN model works well for most clouds in the nighttime and the retrieval results agree reasonably well with the spatial distribution of BT (Fig. 4b and c). High COT retrievals occur in regions with relatively low BT values (Fig. 4d), which is consistent with the fact that thicker clouds are able to block more surface thermal radiance than thin clouds. According to Fig. 4e, the CER retrieval values are higher over regions covered by higher clouds (such as the right region), which is consistent with the fact that high clouds are usually formed by larger ice cloud crystals. The CTH retrieval results are also similarly distributed with the same patterns as the BT (Fig. 4f).

3.2. Daytime quantitative evaluation against MODIS products

After checking the performance of the CNN model by visual, further quantitative evaluations for daytime performance are implemented against standard MODIS cloud products. As the TIR-CNN can retrieve cloud properties for all identified cloud pixels, while some missing values exist in MODIS cloud products, the performance evaluations are applied for those with successful retrievals from the standard MODIS

cloud products. Fig. 5 shows the pixel-to-pixel quantitative evaluations of the TIR-CNN algorithm in 2009. According to Fig. 5 (a, d, g), the three CNN-retrieved cloud properties overall agree well with the MYD06 products. All COT retrieved from the TIR-CNN model is consistent well with MYD06 products with R of 0.790, RMSE of 7.924, and MBE of -0.621, respectively. The COT results obtain optimal solutions in the estimations smaller than 15 and are uniformly distributed around the one-to-one line in the range of 0 to 30. The MBE, RMSE, and R of all available CER are -0.696 μm, 5.512 μm, and 0.845, respectively. The largest probability density occurs in the region with CER smaller than 20 μm. For CTH retrievals, the CNN-MODIS matchups are densely located near the 1:1 line with small estimation differences (MBE = -0.068 km, RMSE = 1.305 km, and R = 0.954). Compared with two independent cloud products (i.e., MYD06 and CERES-MODIS), the TIR-CNN RMSE errors are not large compared to the baseline errors inferred from two cloud products (Fig. S14).

It is worth noting that the retrieval bias in the MODIS cloud products is higher when the solar zenith angle (SZA) is large (Grosvenor and Wood, 2014), so the evaluations are further quantified with low SZA ($< 60^\circ$) results, as shown in Fig. 5 (b, e, h). Under the SZA constriction, all the statistical metrics for these three products are improved significantly

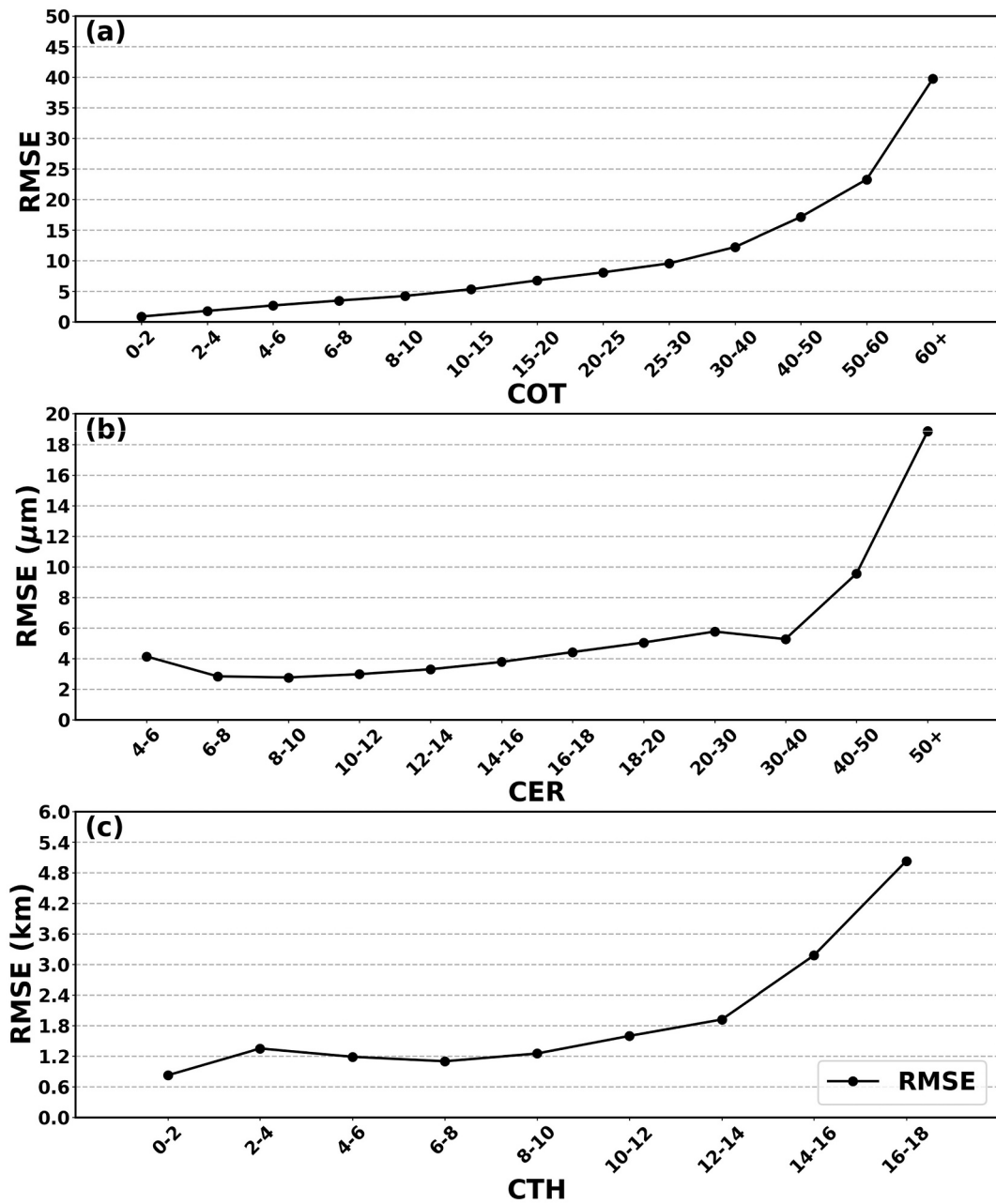


Fig. 6. The RMSE of COT (a), CER (b), and CTH (c) as the functions of different value ranges.

(Fig. 5b, e, h). The right column (Fig. 5c, f, i) depicts the probability density functions of two products with SZA constrained, it can be concluded that CNN-retrieved cloud properties are similar to those obtained by standard MODIS cloud products, with some small differences.

Further estimations are performed to explore the performance of the TIR-CNN model as a function of the range of cloud property values. As shown in Fig. 6, the error analyses indicate that the TIR-CNN model can retrieve the COT smaller than 40 with relatively small RMSE. The TIR-CNN model performs best for CER over the prescribed range ($< 40 \mu\text{m}$), where RMSE are often below 6 μm (Fig. 6b). As there are fewer samples with CER $< 6 \mu\text{m}$, the present model performs relatively poorly in this range resulting in a slight increase in RMSE. From Fig. 6c, optimal CTH retrievals are derived for almost all clouds, except for errors slightly increasing in high ($> 14 \text{ km}$) clouds. Fig. S15 gives the detailed contributions of each variable in the cloud property retrievals. In COT predictions, bands 29, 33, and 35 make greater contributions than other bands (Fig. S15a). Bands 29 and 35 play the most important roles in

retrieving COT larger than 20 and between 2 and 8, respectively. For CER (Fig. S15b), bands 29, 33, and 34 contribute more than 60% in the range of 4-10 μm , while bands 29, 32, and 34 make similar contributions in 10-18 μm . The most important three channels are bands 31, 32, and 33 when CER $> 20 \mu\text{m}$. From Fig. S15c, bands 29 and 31, band 32, and band 33 make the largest contributions in retrieving CTH located at 0-6 km, 6-12 km, and 12-18 km height, respectively.

3.3. Nighttime quantitative evaluation against CALIPSO products

In nighttime scenes, cloud optical properties can not be collected from standard MYD06 cloud products, the near-real-time measurements from the CALIPSO Level 2 1 km cloud layer products are used to complement the nighttime evaluation. Single-layer measurements from CALIPSO are matched with MODIS observations by limiting the distance to smaller than 333 m (distance between adjacent CALIPSO footprints), with the time difference smaller than 90 s. These spatially and

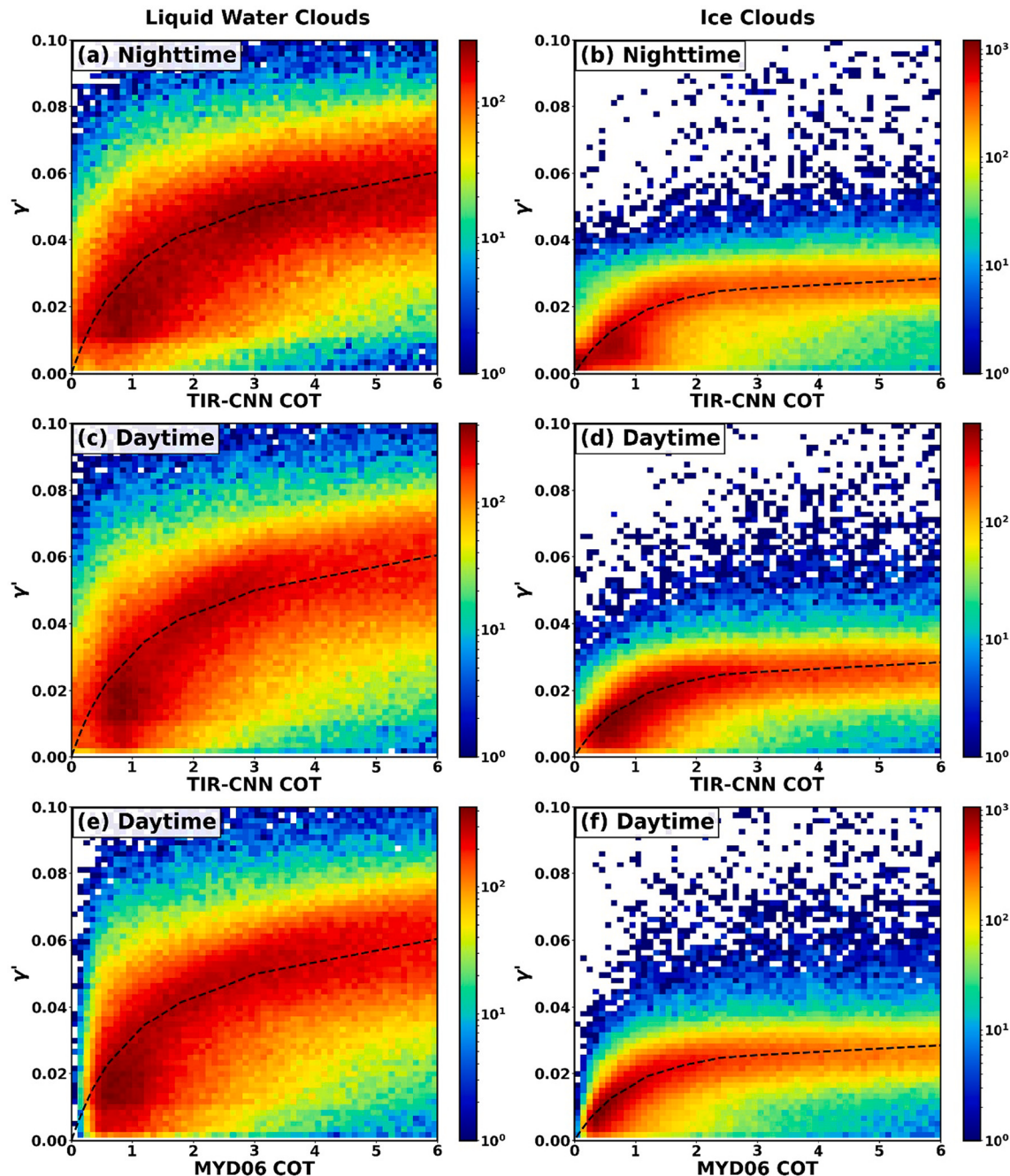


Fig. 7. Pixel-by-pixel comparisons of CNN/MODIS-derived COT with layer-integrated backscatter from CALIPSO products in 2009. Only single-layer clouds are used in these plots. Colors denote the number of observations in each respective pixel, and the dashed lines denote the theoretical relationship between backscatter and COT implied by idealized Monte Carlo radiative transfer simulations. The left column (a, c, e) shows the density scatter plots for liquid water clouds, and the right column (b, d, f) shows ice cloud comparisons. (a-b) are density scatter plots in the nighttime. (c-d) and (e-f) are density scatter plots of the TIR-CNN retrieval results and the MODIS products compared with the CALIPSO products in the daytime, respectively.

temporally co-located samples in 2009 are used to investigate the performance and generalization of the TIR-CNN model in nighttime conditions (Fig. 7).

In this study, the derived COT results are compared with the layer-integrated attenuated backscatter (γ') from CALIPSO. We prefer to indirectly compare the day-time and night-time $\tau\cdot\gamma'$ relationships instead of direct $\tau\cdot\tau$ comparisons, considering the limitation of the CALIOP optical depth dataset. The laser emitted by CALIOP cannot penetrate thick clouds, so it could only retrieve the optical depth of thin clouds (i.e., $\tau < 3$). Furthermore, the spatial resolution of the CALIOP optical depth product is 5 km, which is much larger than those of MODIS

with a spatial resolution of 1 km, so it is inconvenient to compare our derived COT with CALIPSO τ products. The estimations are separately assessed for liquid water clouds and ice clouds according to the cloud phase classifications in CALIPSO products. The theoretical relationship between γ' and τ for both liquid water and ice clouds for CALIPSO is simulated using a Monte Carlo model. In the simulation, the scattering properties of water clouds (effective radius is set to be 10 μm) are calculated with Mie theory, and the scattering properties of ice clouds (the effective particle radius is set to be 30 μm , the ice cloud particle habit is the same as Ding et al. (2016), and the proportion of smooth ice cloud particles is set to be 7%) is calculated with improved geometric

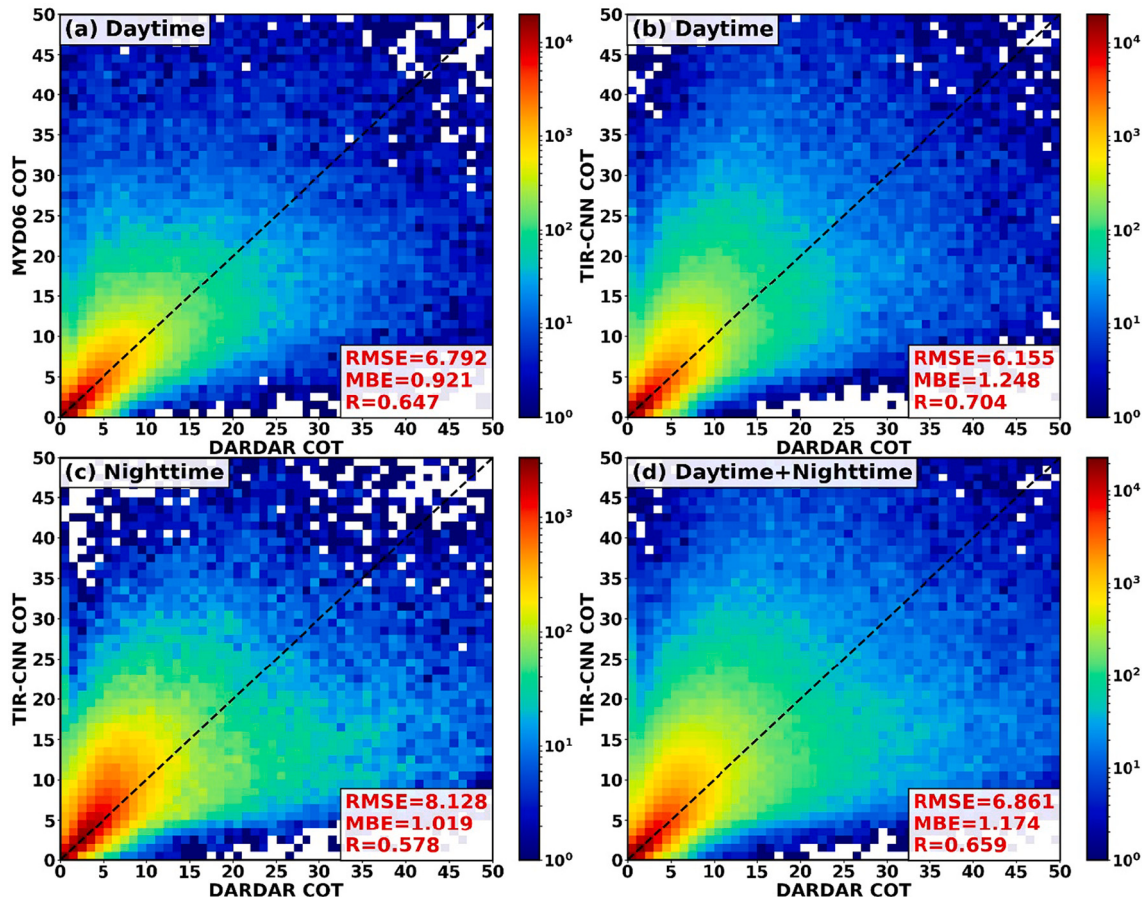


Fig. 8. Comparisons of MODIS COT, CNN-derived COT, and DARDAR for pure ice clouds. The COT comparisons are collected with the latitude in the range of 60°N–60°S for fair comparisons in daytime and nighttime. (a) is the MYD06 COT comparison with DARDAR products in the daytime. (b) is the CNN-retrieved COT (same pixels with the MYD06 COT) comparison with DARDAR products in the daytime. (c) is the CNN-retrieved COT comparison with DARDAR products in the nighttime. (d) is the CNN-retrieved COT comparison with DARDAR products in both daytime and nighttime.

optical method (IGOM, Yang and Liou, 1996). Considering that the coherent backscatter enhancement (Zhou, 2018) is not fully accounted for in IGOM, the backscattering phase function of ice cloud particles is adjusted with the empirical equation of Zhou and Yang (2015). In addition, the geometric thicknesses of a liquid water cloud and an ice cloud are set to be 0.3 and 3 km, respectively. The simulated τ - γ' relationships (black dash line) are then compared with the MODIS-CALIPSO matchups and infer the nighttime performance. According to Fig. 7(a-b), the statistical τ - γ' relationship obtained from the TIR-CNN model and CALIPSO observations consist well with the theoretical relationship implied by the Monte Carlo simulations. Daytime comparisons of the CNN-derived COT and standard MODIS products with CALIPSO measurements are also performed in this study (Fig. 7 c-f), with distribution patterns similar to the nighttime comparison.

The daytime and nighttime ice cloud COT retrievals are also compared with an ice-cloud product that combines the CloudSat radar and the CALIPSO lidar (DARDAR, Delanoë and Hogan, 2010). As shown in Fig. 8, the distributions are similar for all subplots. According to Fig. 8a and b, the COT retrieved by the TIR-CNN is competitive against that from MYD06 products when compared with DARDAR products in the daytime, with RMSE of 6.155 and 6.792, respectively. The RMSE of night-time COT retrievals is 20% greater than the reference daytime RMSE between MYD06 and DARDAR, and is 32% larger than daytime RMSE errors of the TIR-CNN model (Fig. 8c). One possible reason is that the statistical relationships between COT and radiances of adjacent pixels are slightly different during the daytime and nighttime. The MBE of night-time COT is small, indicating that our retrieval can be approximately viewed as an unbiased estimator for both day-time and

night-time, which is important for datasets used in climate studies. The overall RMSE between TIR-CNN and DARDAR COT is very close to that between MYD06 and DARDAR (Fig. 8a and d).

For the nighttime CTH evaluations, retrievals from the TIR-CNN model are compared with the CTH from MYD06 and the CTH of the highest cloud in each profile observed by CALIPSO. Fig. 9a shows that the CTH retrieved by the TIR-CNN model agrees reasonably well with MYD06 products as all three metrics indicate high retrieval quality (i.e. MBE = -0.411 km, RMSE = 1.542 km, and R = 0.937). Both the CNN-retrieved CTH and MYD06 CTH are well consistent with CALIPSO-observed CTH at night (Fig. 9c and e), with similar statistical results (R = 0.861 for TIR-CNN, R = 0.855 for MYD06). The probability density functions of CTH retrievals are shown in the right column of Fig. 9, indicating that the TIR-CNN results achieve comparable and consistent performance in nighttime conditions.

3.4. Spatiotemporal performance

Fig. 10 shows the daily performance of the TIR-CNN model as a function of the day in 2009. The number of obtained granules with a 10-day interval ranges from 125 to 134, with an average number of 130. In general, these results illustrate that the TIR-CNN model can well capture the cloud properties on a daily level, and the time-series fluctuations may be caused by the unevenly distributed data in the polar regions.

To evaluate the performance of the TIR-CNN model from the global point of view, the retrievals in 2009 that are successfully derived in both two products and with $SZA < 60^\circ$ are further aggregated into the global $1^\circ \times 1^\circ$ grids. Fig. 11 shows the global average distributions of CNN-

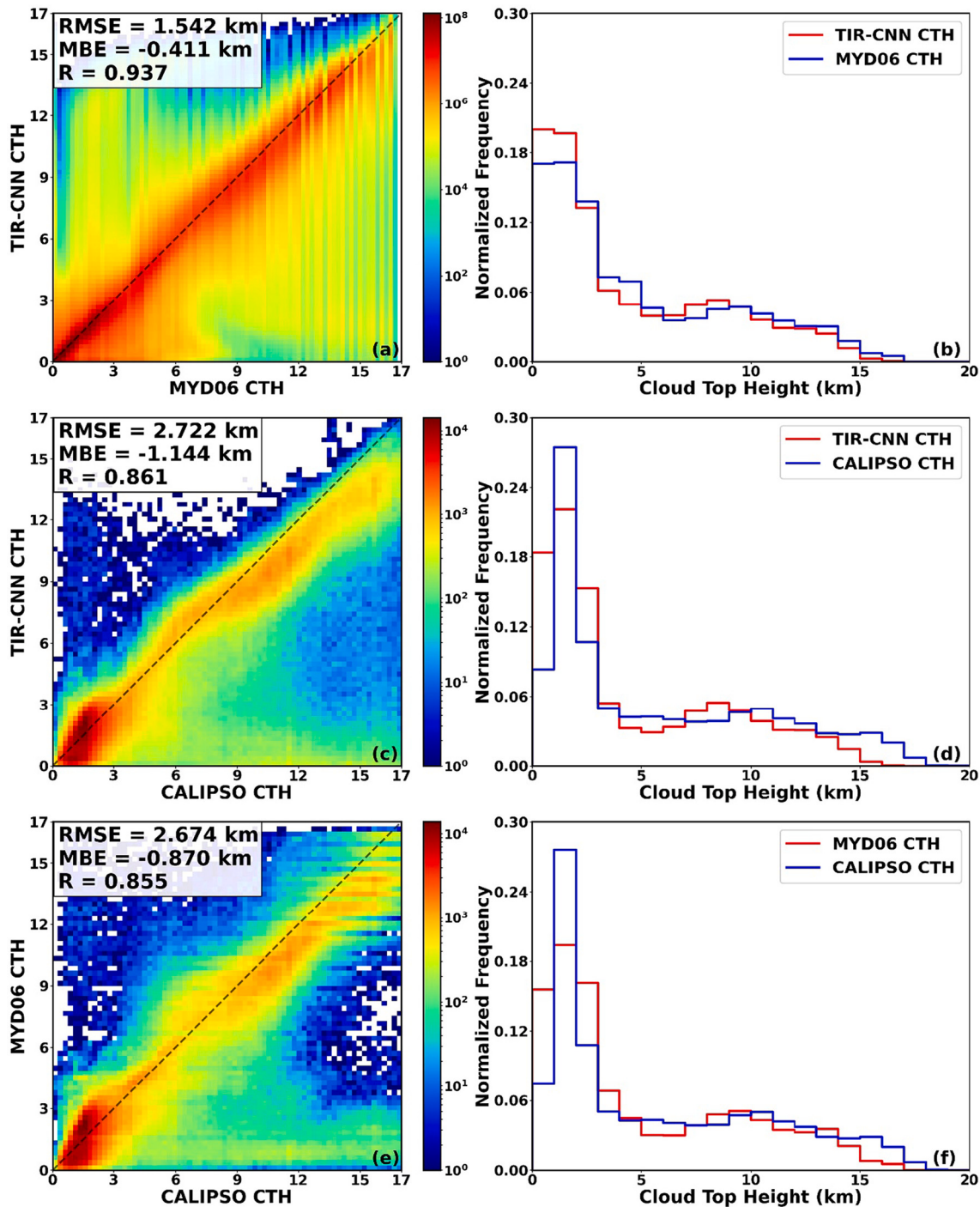


Fig. 9. Density scatter plots and the histograms of the CTH comparisons in the nighttime of 2009. (a) is the CNN-derived CTH comparison with MYD06 products. (c) is the CNN-derived CTH comparison with CALIPSO products. (e) is the CTH from MYD06 products in comparison with CALIPSO products. (b, d, and f) are the corresponding probability density functions.

retrieved COT, CER, and CTH (Fig. 11a-c) and the standard MYD06 cloud products (Fig. 11d-f), as well as their differences (Fig. 11g-i). At first glance, the global mean cloud properties derived from the TIR-CNN model show similar distributions to those from MYD06 products. Fig. 11 (a, d, g) shows that the COT discrepancies over higher-latitude regions are relatively larger than over the tropical ocean, especially within the Arctic Circle, the high-latitude Southern Ocean, and Antarctica, which may be caused by the sun angle or the underlying surface. The mean underestimation of COT is -0.326 . At the global scale, the CNN-retrieved CER is slightly smaller than that from MYD06 products over

the tropical and polar regions except in mid-latitude regions with opposite performance (Fig. 11b, e, and h). The CER underestimations usually occur where the surface temperature is low or the clouds are optically thin as depicted in the COT comparison, with an overall underestimation of $-0.880 \mu\text{m}$. Fig. 11(c, f, i) show that the CTH distribution pattern of CNN-retrieved results is consistent with the MYD06 products over the world with a small discrepancy of -0.081 km . The CTH biases are relatively larger over extremely hot (the Sahara Desert) and cold regions (Greenland and Antarctica).

Fig. 12 shows the global distributions of RMSE (Fig. 12a, c, e) and R

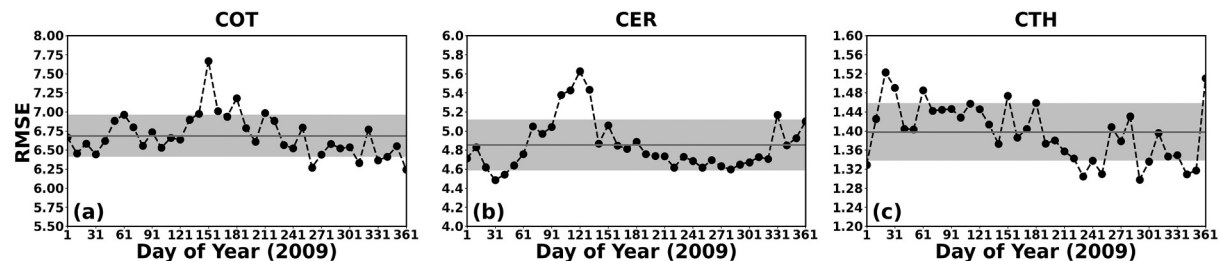


Fig. 10. Daily performance of the TIR-CNN model in terms of RMSE, which are shown as the functions of the day in 2009 with 10-day intervals. In each panel, the black solid line is the mean-value line, and the gray shaded area represents the standard deviation of the time-series evaluation metric.

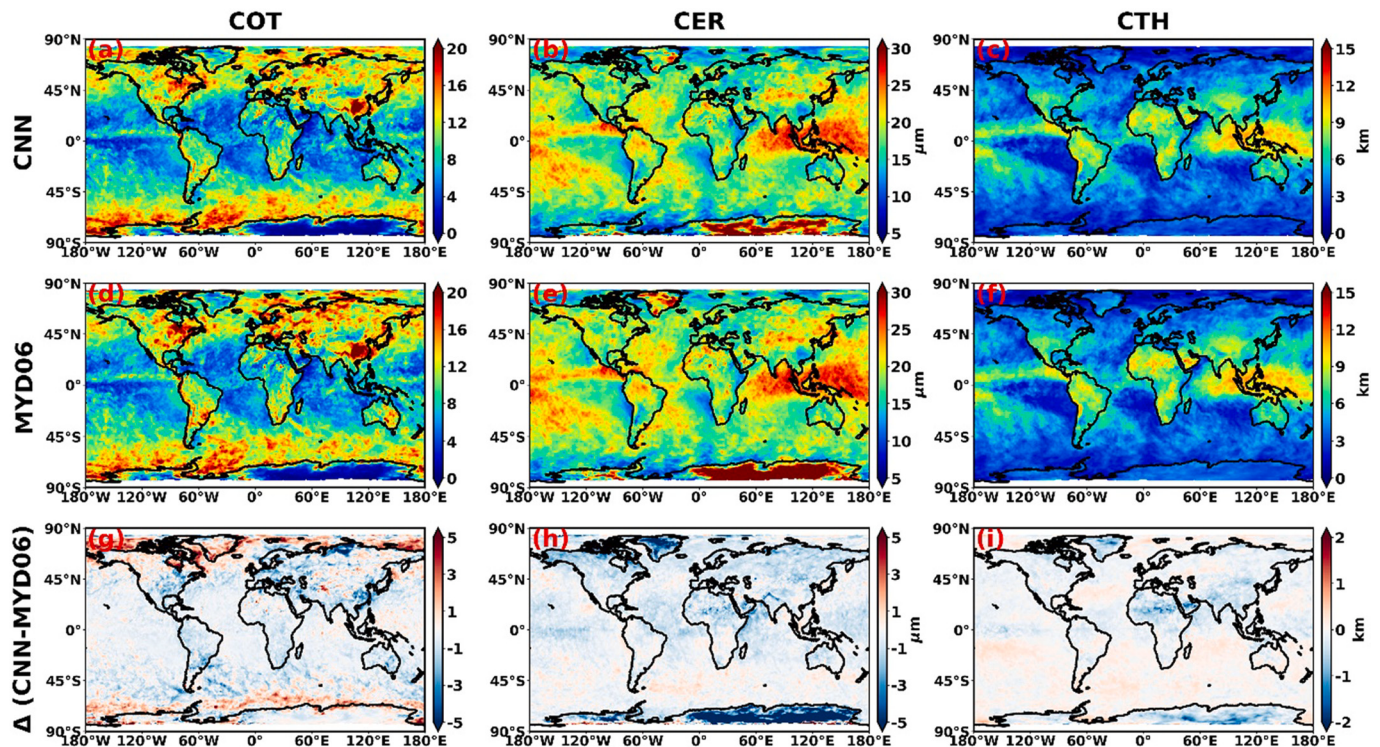


Fig. 11. The global distributions of average COT, CER, and CTH for 2009 in $1 \times 1^\circ$ grids. The retrievals that are successfully derived in both CNN and MYD06 products and with $SZA < 60^\circ$ are collected to calculate the global mean distributions. The first row shows the retrieval results from the TIR-CNN model (a, b, c), the middle row shows the corresponding MYD06 products (d, e, f), and the third row shows the differences between the two results (g, h, i).

(Fig. 12b, d, f) that are calculated with the TIR-CNN retrievals and the standard MYD06 products. The global RMSE distributions have similar distribution patterns compared with Fig. 11. The errors of COT are relatively small in low-value regions (45°N - 45°S region) and increase in larger value regions (Fig. 12a). According to Fig. 11g, high errors usually occur in regions with high COT. The mean RMSE of COT at the global scale is 6.38. From Fig. 12c, we can see that the CNN-derived CER presents a relatively smaller RMSE over the ocean than that over land. The mean RMSE of CER is $5.17 \mu\text{m}$. These retrieval errors are mainly caused by the underestimations revealed in Fig. 11h. The results in Fig. 12e show that the RMSE (mean = 1.19 km) of CTH over the globe is slightly small except for the high cloud coverages. Meanwhile, the global correlation coefficient distributions of three cloud products (Fig. 12b, d, and f) give evidence of the relatively high precision and robustness of the TIR-CNN model at the global scale, with the mean values of 0.81, 0.83, and 0.93, respectively.

4. Conclusions

In this study, a CNN-based algorithm is developed to retrieve cloud

optical thickness, effective particle radius, and cloud top height in both daytime and nighttime. The TIR-CNN model is trained with solar-independent variables (thermal infrared radiances, viewing zenith angles, and altitude) as inputs and uses standard MYD06 products (solar-dependent retrievals in the daytime) as targets. Then the model is tested by the standard MODIS products and active products, and promising results are found in experimental results and their evaluations.

For daytime performance, the comparisons with MYD06 products show a good correlation for CTH ($R = 0.95$), CER ($R = 0.85$) and COT ($R = 0.79$). Though the RMSE of COT at night-time may decrease, the small biases in the diurnal cycle according to COT-backscatter relationships and DARDAR products indicate it is beneficial for climate studies. Comparisons of CTH retrieved from TIR-CNN, MYD06, and CALIPSO indicate that the CNN trained using day-time observations is reliable in the nighttime for CTH retrievals.

Compared with traditional cloud retrieval methods, the advantage of CNN-based retrievals can be briefly summarized as follows:

- (1) Compared with solar reflectance-based methods, the TIR-CNN model extends the COT and CER retrievals to nighttime

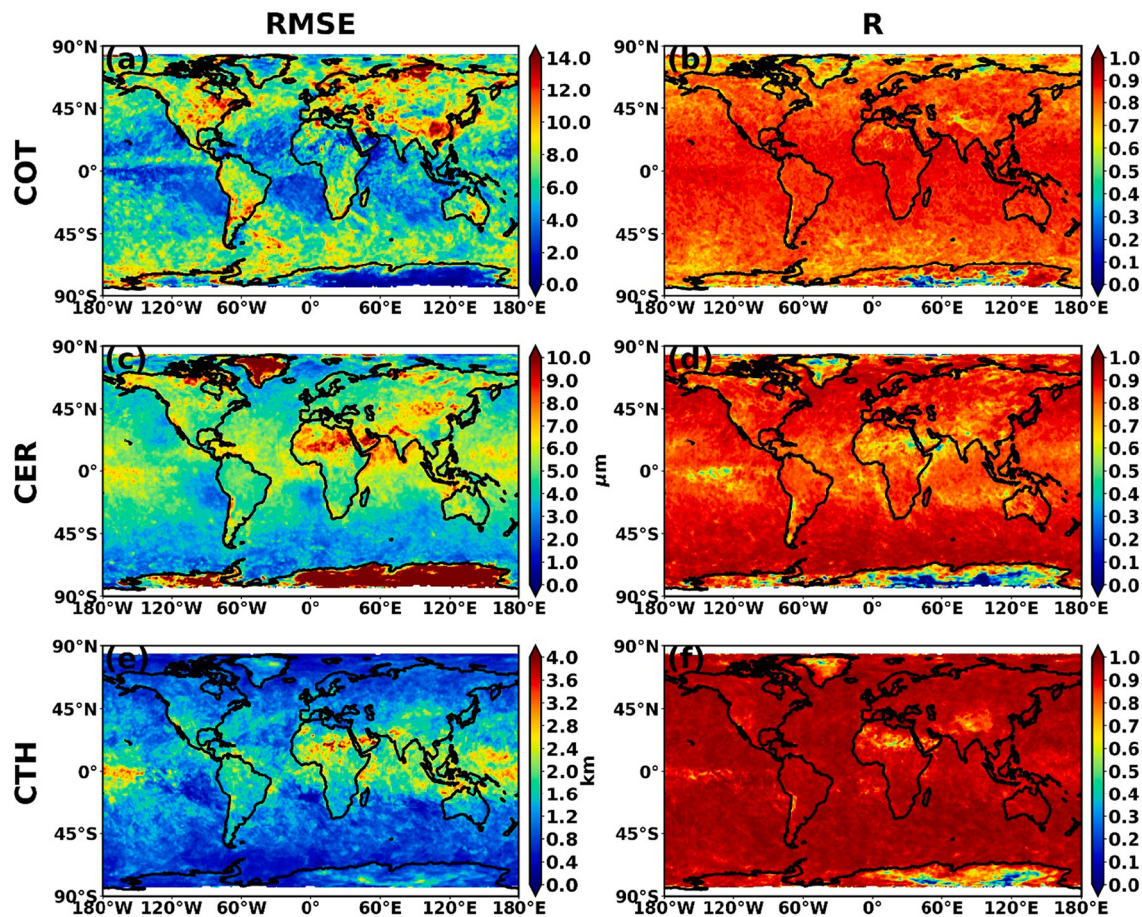


Fig. 12. The spatial distributions ($1 \times 1^\circ$ grid box) of RMSE and R for COT, CER, and CTH between the TIR-CNN model and MYD06 cloud products. The retrievals that are successfully derived in both CNN and MYD06 products and with $SZA < 60^\circ$ are collected to calculate the global distributions of evaluation metrics. The left column (a, c, e) shows the RMSE distributions for COT, CER, and CTH, and the right column (b, d, f) shows the correlation coefficients of the corresponding two products.

conditions. The biases are small for both daytime and nighttime, though the RMSE of COT against DARDAR at nighttime is 32% greater than that at daytime.

- (2) The convolutions in the algorithm are beneficial in considering the information from neighbor fields in training and naturally imputing the missing predictions that failed in the split-window method. The performance of the TIR-CNN model in thick cloud COT retrievals is better than previous TIR-based algorithms (Iwabuchi et al., 2016; Wang et al., 2016a; Libois and Blanchet, 2017). Note that the uncertainties of COT retrievals for thick clouds are greater than that of thin clouds because the thick cloud COT retrievals are primarily based on the spatial distributions of cloud properties, which are inevitably affected by uncertainties.
- (3) The computational cost of our TIR-CNN model is smaller than most traditional IR retrieval methods.
- (4) The TIR-CNN model can achieve satisfactory robustness and generalization without introducing any other auxiliary atmospheric parameters (which is required in OE-IR methods).

The main limitation of the current approach is the quality limitation of training labels from MYD06 cloud products, and it can be improved by the evolving algorithm and standard products update. The diurnal consistency might be further improved by training with data from far-infrared sensors and active sensors in the future. This method can be applied to other passive satellites by retraining the TIR-CNN model with corresponding satellite observations and training datasets. In the future, the performance of this method might be further improved with a

combination of reinforcement learning and traditional physical algorithms (i.e., Wang et al., 2016b) based on radiative transfer calculations.

CRediT authorship contribution statement

Quan Wang: Methodology, Data curation, Validation, Formal analysis. **Chen Zhou:** Conceptualization, Methodology, Validation, Writing – review & editing, Supervision. **Xiaoyong Zhuge:** Writing – review & editing. **Chao Liu:** Writing – review & editing. **Fuzhong Weng:** Writing – review & editing. **Minghuai Wang:** Writing – review & editing.

Declaration of Competing Interest

The authors declare that they have no known competing financial interests or personal relationships that could have appeared to influence the work reported in this paper.

Acknowledgments

This work was supported by the National Natural Science Foundation of China [grant numbers 42075127, 41875095]. The authors would like to thank NASA for freely providing the MODIS (<https://ladsweb.modaps.eosdis.nasa.gov/>), and CALIPSO (<https://search.earthdata.nasa.gov/search>) data online.

Appendix A. Supplementary data

Supplementary data to this article can be found online at <https://doi.org/10.1016/j.rse.2022.113079>.

References

- Baum, B.A., Yang, P., Heymsfield, A.J., Platnick, S., King, M.D., Hu, Y.-X., Bedka, S.T., 2005. Bulk scattering properties for the remote sensing of ice clouds. Part II: narrowband models. *J. Appl. Meteorol. Climatol.* 44 (12), 1896–1911. <https://doi.org/10.1175/JAM2309.1>.
- Baum, B.A., Menzel, W.P., Frey, R.A., Tobin, D.C., Holz, R.E., Ackerman, S.A., Heidinger, A.K., Yang, P., 2012. MODIS cloud-top property refinements for collection 6. *J. Appl. Meteorol. Climatol.* 51 (6), 1145–1163. <https://doi.org/10.1175/JAMC-D-11-0203.1>.
- Boucher, O., Randall, D., Artaxo, P., Bretherton, C., Feingold, G., Forster, P., Kerminen, V.-M., Kondo, Y., Liao, H., Lohmann, U., Rasch, P., Satheesh, S.K., Sherwood, S., Stevens, B., Zhang, X.Y., 2013. Clouds and aerosols. In: Stocker, T.F., Qin, D., Plattner, G.-K., Tignor, M., Allen, S.K., Boschung, J., Nauels, A., Xia, Y., Bex, V., Midgley, P.M. (Eds.), *Climate Change 2013: The Physical Science Basis. Contribution of Working Group I to the Fifth Assessment Report of the Intergovernmental Panel on Climate Change*. Cambridge University Press, Cambridge, United Kingdom and New York, NY, USA.
- Caruana, R., 1997. Multitask learning. *Mach. Learn.* 28, 41–75. <https://doi.org/10.1023/A:1007379606734>.
- Cho, H.M., Zhang, Z., Meyer, K., Lebsack, M., Platnick, S., Ackerman, A.S., Girolamo, L.D., Labonne, C., Cornet, C., Riedi, J., Holz, R.E., 2015. Frequency and causes of failed MODIS cloud property retrievals for liquid phase clouds over global oceans. *J. Geophys. Res.-Atmos.* 120 (9), 4132–4154. <https://doi.org/10.1002/2015JD023161>.
- Delanoë, J., Hogan, R.J., 2010. Combined CloudSat-CALIPSO-MODIS retrievals of the properties of ice clouds. *J. Geophys. Res.-Atmos.* 115 (D4) <https://doi.org/10.1029/2009JD012346>.
- Ding, J., Yang, P., Holz, R.E., Platnick, S., Meyer, K.G., Vaughan, M.A., Hu, Y., King, M.D., 2016. Ice cloud backscatter study and comparison with CALIPSO and MODIS satellite data. *Opt. Express* 24 (1), 620–636. <https://doi.org/10.1364/OE.24.000620>.
- Duda, D.P., Spinhirne, J.D., 1996. Split-window retrieval of particle size and optical depth in contrails located above horizontally inhomogeneous ice clouds. *Geophys. Res. Lett.* 23 (25), 3711–3714. <https://doi.org/10.1029/96GL03645>.
- Fauchez, T., Platnick, S., Sourdeval, O., Wang, C., Meyer, K., Cornet, C., Szczap, F., 2018. Cirrus horizontal heterogeneity and 3-D radiative effects on cloud optical property retrievals from MODIS near to thermal infrared channels as a function of spatial resolution. *J. Geophys. Res.-Atmos.* 123 (19), 11141–11153. <https://doi.org/10.1029/2018JD028726>.
- Gong, J., Zeng, X., Wu, D.L., Li, X., 2018. Diurnal variation of tropical ice cloud microphysics: evidence from global precipitation measurement microwave imager polarimetric measurements. *Geophys. Res. Lett.* 45 (2), 1185–1193. <https://doi.org/10.1002/2017GL075519>.
- Grosvenor, D.P., Wood, R., 2014. The effect of solar zenith angle on MODIS cloud optical and microphysical retrievals within marine liquid water clouds. *Atmos. Chem. Phys.* 14 (14), 7291–7321. <https://doi.org/10.5194/acp-14-7291-2014>.
- Håkansson, N., Adok, C., Thoss, A., Scheirer, R., Hörnquist, S., 2018. Neural network cloud top pressure and height for MODIS. *Atmos. Meas. Tech.* 11 (5), 3177–3196. <https://doi.org/10.5194/amt-11-3177-2018>.
- Hamada, A., Nishi, N., 2010. Development of a cloud-top height estimation method by geostationary satellite split-window measurements trained with CloudSat data. *J. Appl. Meteorol. Climatol.* 49 (9), 2035–2049. <https://doi.org/10.1175/2010JAMC2287.1>.
- He, K., Zhang, X., Ren, S., Sun, J., 2015. Delving Deep into Rectifiers: Surpassing Human-Level Performance on ImageNet Classification arXiv:1502.01852 [cs].
- Heidinger, A.K., Pavolonis, M.J., 2009. Gazing at cirrus clouds for 25 years through a split window. Part I: methodology. *J. Appl. Meteorol. Climatol.* 48 (6), 1100–1116. <https://doi.org/10.1175/2008JAMC1882.1>.
- Inoue, T., 1985. On the temperature and effective emissivity determination of semi-transparent cirrus clouds by bi-spectral measurements in the 10 μ m window region. *J. Meteorol. Soc. Jpn. Ser. II* 63 (1), 88–99. <https://doi.org/10.2151/jmsj1965.63.1.88>.
- Iwabuchi, H., Hayasaka, T., 2003. A multi-spectral non-local method for retrieval of boundary layer cloud properties from optical remote sensing data. *Remote Sens. Environ.* 88 (3), 294–308. <https://doi.org/10.1016/j.rse.2003.08.005>.
- Iwabuchi, H., Yamada, S., Katagiri, S., Yang, P., Okamoto, H., 2014. Radiative and microphysical properties of cirrus cloud inferred from infrared measurements made by the moderate resolution imaging spectroradiometer (MODIS). Part I: retrieval method. *J. Appl. Meteorol. Climatol.* 53 (5), 1297–1316. <https://doi.org/10.1175/JAMC-D-13-0215.1>.
- Iwabuchi, H., Saito, M., Tokoro, Y., Putri, N.S., Sekiguchi, M., 2016. Retrieval of radiative and microphysical properties of clouds from multispectral infrared measurements. *Prog. Earth Planet. Sci.* 3, 32. <https://doi.org/10.1186/s40645-016-0108-3>.
- Iwabuchi, H., Putri, N.S., Saito, M., Tokoro, Y., Sekiguchi, M., Yang, P., Baum, B.A., 2018. Cloud property retrieval from multiband infrared measurements by Himawari-8. *J. Meteorol. Soc. Jpn. Ser. II* 96B, 27–42. <https://doi.org/10.2151/jmsj.2018-001>.
- Kiehl, J.T., Hack, J.J., Briegleb, B.P., 1994. The simulated earth radiation budget of the National center for atmospheric research community climate model CCM2 and comparisons with the earth radiation budget experiment (ERBE). *J. Geophys. Res.-Atmos.* 99 (D10), 20815–20827. <https://doi.org/10.1029/94JD00941>.
- King, M.D., Kaufman, Y.J., Menzel, W.P., Tanre, D., 1992. Remote sensing of cloud, aerosol, and water vapor properties from the moderate resolution imaging spectrometer (MODIS). *IEEE Trans. Geosci. Remote Sens.* 30 (1), 2–27. <https://doi.org/10.1109/36.124212>.
- King, M.D., Menzel, W.P., Kaufman, Y.J., Tanre, D., Gao, B.-C., Platnick, S., Ackerman, S.A., Remer, L.A., Pincus, R., Hubanks, P.A., 2003. Cloud and aerosol properties, precipitable water, and profiles of temperature and water vapor from MODIS. *IEEE Trans. Geosci. Remote Sens.* 41 (2), 442–458. <https://doi.org/10.1109/TGRS.2002.808226>.
- Kingma, D.P., Ba, J., 2014. Adam: A Method for Stochastic Optimization arXiv: 1412.6980 [cs].
- Lai, R., Teng, S., Yi, B., Letu, H., Min, M., Tang, S., Liu, C., 2019. Comparison of cloud properties from Himawari-8 and FengYun-4A geostationary satellite radiometers with MODIS cloud retrievals. *Remote Sens.* 11 (14), 1703. <https://doi.org/10.3390/rs11141703>.
- Lang, N., Schindler, K., Wegner, J.D., 2019. Country-wide high-resolution vegetation height mapping with Sentinel-2. *Remote Sens. Environ.* 233, 111347 <https://doi.org/10.1016/j.rse.2019.111347>.
- Leinonen, J., Guillaume, A., Yuan, T., 2019. Reconstruction of cloud vertical structure with a generative adversarial network. *Geophys. Res. Lett.* 46, 7035–7044. <https://doi.org/10.1029/2019GL082532>.
- Letu, H., Yang, K., Nakajima, T.Y., Ishimoto, H., Nagao, T.M., Riedi, J., Baran, A.J., Ma, R., Wang, T., Shang, H., Khatri, P., Chen, L., Shi, C., Shi, J., 2020. High-resolution retrieval of cloud microphysical properties and surface solar radiation using Himawari-8/AHI next-generation geostationary satellite. *Remote Sens. Environ.* 239, 111583 <https://doi.org/10.1016/j.rse.2019.111583>.
- Li, L., Franklin, M., Girguis, M., Lurmann, F., Wu, J., Pavlovic, N., Breton, C., Gilliland, F., Habre, R., 2020. Spatiotemporal imputation of MAIAC AOD using deep learning with downscaling. *Remote Sens. Environ.* 237, 111584 <https://doi.org/10.1016/j.rse.2019.111584>.
- Libois, Q., Blanchet, J.P., 2017. Added value of far-infrared radiometry for remote sensing of ice clouds. *J. Geophys. Res.-Atmos.* 122 (12), 6541–6564. <https://doi.org/10.1020/2016JD026423>.
- Long, J., Shelhamer, E., Darrell, T., 2015. Fully convolutional networks for semantic segmentation 2015 IEEE Conference on Computer Vision and Pattern Recognition (CVPR), pp 3431–3440. <https://doi.org/10.1109/CVPR.2015.7298965>.
- Marchand, R., Ackerman, T., Smyth, M., Rossow, W.B., 2010. A review of cloud top height and optical depth histograms from MISR, ISCCP, and MODIS. *J. Geophys. Res.-Atmos.* 115 (D16) <https://doi.org/10.1029/2009JD013423>.
- Menzel, W.P., Frey, R.A., Zhang, H., Wylie, D.P., Moeller, C.C., Holz, R.E., Maddux, B., Baum, B.A., Strabala, K.I., Gumley, L.E., 2008. MODIS global cloud-top pressure and amount estimation: algorithm description and results. *J. Appl. Meteorol. Climatol.* 47 (4), 1175–1198. <https://doi.org/10.1175/2007JAMC1705.1>.
- Min, M., Li, J., Wang, F., Liu, Z., Menzel, W.P., 2020. Retrieval of cloud top properties from advanced geostationary satellite imager measurements based on machine learning algorithms. *Remote Sens. Environ.* 239, 111616 <https://doi.org/10.1016/j.rse.2019.111616>.
- Minnis, P., Sun-Mack, S., Young, D.F., Heck, P.W., Garber, D.P., Chen, Y., Spangenberg, D.A., Arduini, R.F., Trepte, Q.Z., Smith, W.L., Ayers, J.K., Gibson, S.C., Miller, W.H., Hong, G., Chakrapani, V., Takano, Y., Liou, K.-N., Xie, Y., Yang, P., 2011. CERES edition-2 cloud property retrievals using TRMM VIRS and terra and aqua MODIS data—part I: algorithms. *IEEE Trans. Geosci. Remote Sens.* 49 (11), 4374–4400. <https://doi.org/10.1109/TGRS.2011.2144601>.
- Minnis, P., Sun-Mack, S., Chen, Y., Chang, F.-L., Yost, C.R., Smith, W.L., Heck, P.W., Arduini, R.F., Bedka, S.T., Yi, Y., Hong, G., Jin, Z., Painemal, D., Palikonda, R., Scarino, B.R., Spangenberg, D.A., Smith, R.A., Trepte, Q.Z., Yang, P., Xie, Y., 2021. CERES MODIS cloud product retrievals for edition 4—part I: algorithm changes. *IEEE Trans. Geosci. Remote Sens.* 59 (4), 2744–2780. <https://doi.org/10.1109/TGRS.2020.3008866>.
- Nakajima, T., King, M.D., 1990. Determination of the optical thickness and effective particle radius of clouds from reflected solar radiation measurements. Part I: theory. *J. Atmos. Sci.* 47 (15), 1878–1893. [https://doi.org/10.1175/1520-0469\(1990\)047<1878:DOTOTA>2.0.CO;2](https://doi.org/10.1175/1520-0469(1990)047<1878:DOTOTA>2.0.CO;2).
- Nauss, T., Kokhanovsky, A.A., 2011. Retrieval of warm cloud optical properties using simple approximations. *Remote Sens. Environ.* 115 (6), 1317–1325. <https://doi.org/10.1016/j.rse.2011.01.010>.
- Parol, F., Buriez, J.C., Brogniez, G., Fouquart, Y., 1991. Information content of AVHRR channels 4 and 5 with respect to the effective radius of cirrus cloud particles. *J. Appl. Meteorol. Climatol.* 30 (7), 973–984. <https://doi.org/10.1175/1520-0450-30.7.973>.
- Platnick, S., Li, J.Y., King, M.D., Gerber, H., Hobbs, P.V., 2001. A solar reflectance method for retrieving the optical thickness and droplet size of liquid water clouds over snow and ice surfaces. *J. Geophys. Res.-Atmos.* 106 (D14), 15185–15199. <https://doi.org/10.1029/2000JD900441>.
- Platnick, S., King, M.D., Ackerman, S.A., Menzel, W.P., Baum, B.A., Riedi, J.C., Frey, R.A., 2003. The MODIS cloud products: algorithms and examples from Terra. *IEEE Trans. Geosci. Remote Sens.* 41, 459–473. <https://doi.org/10.1109/TGRS.2002.808301>.
- Platnick, S., Meyer, K.G., King, M.D., Wind, G., Amarasinghe, N., Marchant, B., Arnold, G.T., Zhang, Z., Hubanks, P.A., Holz, R.E., Yang, P., Ridgway, W.L., Riedi, J., 2017. The MODIS cloud optical and microphysical products: collection 6 updates and examples from terra and aqua. *IEEE Trans. Geosci. Remote Sens.* 55 (1), 502–525. <https://doi.org/10.1109/TGRS.2016.2610522>.

- Rakwatin, P., Takeuchi, W., Yasuoka, Y., 2007. Stripe noise reduction in MODIS data by combining histogram matching with facet filter. *IEEE Trans. Geosci. Remote Sens.* 45 (6), 1844–1856. <https://doi.org/10.1109/TGRS.2007.895841>.
- Ronneberger, O., Fischer, P., Brox, T., 2015. U-Net: Convolutional networks for biomedical image segmentation. In: Navab, N., Hornegger, J., Wells, W.M., Frangi, A.F. (Eds.), *Medical Image Computing and Computer-Assisted Intervention - MICCAI 2015*, Lecture Notes in Computer Science. Springer International Publishing, Cham, pp. 234–241. https://doi.org/10.1007/978-3-319-24574-4_28.
- Saito, M., Iwabuchi, H., Yang, P., Tang, G., King, M.D., Sekiguchi, M., 2017. Ice particle morphology and microphysical properties of cirrus clouds inferred from combined CALIOP-IIR measurements. *J. Geophys. Res.-Atmos.* 122, 4440–4462. <https://doi.org/10.1002/2016JD026080>.
- Saito, M., Yang, P., Huang, X., Brindley, H.E., Mlynczak, M.G., Kahn, B.H., 2020. Spaceborne middle- and far-infrared observations improving nighttime ice cloud property retrievals. *Geophys. Res. Lett.* 47 (18) <https://doi.org/10.1029/2020GL087491> e2020GL087491.
- Stevens, B., Bony, S., 2013. What are climate models missing? *Science* 340 (6136), 1053–1054. <https://doi.org/10.1126/science.1237554>.
- Tang, G., Panetta, R.L., Yang, P., Kattawar, G.W., Zhai, P.-W., 2017. Effects of ice crystal surface roughness and air bubble inclusions on cirrus cloud radiative properties from remote sensing perspective. *J. Quant. Spectrosc. Radiative Transf. Laser-Light Interact. Part.* 195, 119–131. <https://doi.org/10.1016/j.jqsrt.2017.01.016>.
- Teng, S., Liu, C., Zhang, Z., Wang, Y., Sohn, B.J., Yung, Y.L., 2020. Retrieval of ice-over-water cloud microphysical and optical properties using passive radiometers. *Geophys. Res. Lett.* 47 (16) <https://doi.org/10.1029/2020GL088941> e2020GL088941.
- Twomey, S., Cocks, T., 1982. Spectral reflectance of clouds in the near-infrared: comparison of measurements and calculations. *J. Meteorol. Soc. Jpn. Ser. II* 60 (1), 583–592. https://doi.org/10.2151/jmsj1965.60.1_583.
- Wang, C., Platnick, S., Zhang, Z., Meyer, K., Wind, G., Yang, P., 2016a. Retrieval of ice cloud properties using an optimal estimation algorithm and MODIS infrared observations: 2. Retrieval evaluation. *J. Geophys. Res.-Atmos.* 121, 5827–5845. <https://doi.org/10.1002/2015JD024528>.
- Wang, C., Platnick, S., Zhang, Z., Meyer, K., Yang, P., 2016b. Retrieval of ice cloud properties using an optimal estimation algorithm and MODIS infrared observations: 1. Forward model, error analysis, and information content. *J. Geophys. Res.-Atmos.* 121, 5809–5826. <https://doi.org/10.1002/2015JD024526>.
- Wang, C., Platnick, S., Meyer, K., Zhang, Z., Zhou, Y., 2020. A machine-learning-based cloud detection and thermodynamic-phase classification algorithm using passive spectral observations. *Atmos. Meas. Tech.* 13 (5), 2257–2277. <https://doi.org/10.5194/amt-13-2257-2020>.
- Wieland, M., Li, Y., Martinis, S., 2019. Multi-sensor cloud and cloud shadow segmentation with a convolutional neural network. *Remote Sens. Environ.* 230, 111203 <https://doi.org/10.1016/j.rse.2019.05.022>.
- Winker, D.M., Hunt, W.H., McGill, M.J., 2007. Initial performance assessment of CALIOP. *Geophys. Res. Lett.* 34 (19) <https://doi.org/10.1029/2007GL030135>.
- Yang, P., Liou, K.N., 1996. Geometric-optics-integral-equation method for light scattering by nonspherical ice crystals. *Appl. Opt.* 35 (33), 6568–6584. <https://doi.org/10.1364/AO.35.006568>.
- Yang, P., Tsay, S.C., Wei, H., Guo, G., Ji, Q., 2005. Remote sensing of cirrus optical and microphysical properties from ground-based infrared radiometric measurements—part I: a new retrieval method based on microwindow spectral signature. *IEEE Geosci. Remote Sens. Lett.* 2 (2), 128–131. <https://doi.org/10.1109/LGRS.2005.844733>.
- Yang, P., Liou, K.-N., Bi, L., Liu, C., Yi, B., Baum, B.A., 2015. On the radiative properties of ice clouds: light scattering, remote sensing, and radiation parameterization. *Adv. Atmos. Sci.* 32, 32–63. <https://doi.org/10.1007/s00376-014-0011-z>.
- Yuan, Q., Shen, H., Li, T., Li, Z., Li, S., Jiang, Y., Xu, H., Tan, W., Yang, Q., Wang, J., Gao, J., Zhang, L., 2020. Deep learning in environmental remote sensing: achievements and challenges. *Remote Sens. Environ.* 241, 111716 <https://doi.org/10.1016/j.rse.2020.111716>.
- Zhang, F., Wu, K., Li, J., Zhang, H., Hu, S., 2018. Radiative transfer in the region with solar and infrared spectra overlap. *J. Quant. Spectrosc. Radiat. Transf.* 219, 366–378. <https://doi.org/10.1016/j.jqsrt.2018.08.025>.
- Zhou, C., 2018. Coherent backscatter enhancement in single scattering. *Opt. Express* 26 (10), A508–A519. <https://doi.org/10.1364/OE.26.00A508>.
- Zhou, C., Yang, P., 2015. Backscattering peak of ice cloud particles. *Opt. Express* 23 (9), 11995–12003. <https://doi.org/10.1364/OE.23.011995>.
- Zhuge, X., Zou, X., Wang, Y., 2021. AHI-derived daytime cloud optical/microphysical properties and their evaluations with the collection-6.1 MOD06 product. *IEEE Trans. Geosci. Remote Sens.* 59 (8), 6431–6450. <https://doi.org/10.1109/TGRS.2020.3027017>.